The International Journal of Advanced Manufacturing Technology (2019) 104:4091–4104
https://doi.org/10.1007/s00170-019-04177-0

ORIGINAL ARTICLE

Surface quality monitoring in abrasive water jet machining of Ti6Al4V–CFRP stacks through wavelet packet analysis of acoustic emission signals

Rishi Pahuja[1] · **M. Ramulu**[1]

Received: 25 April 2019 / Accepted: 17 July 2019 / Published online: 29 July 2019

Abstract

Machining such as trimming and drilling of aerospace composite structures is often required to meet the intended geometric tolerances and functional requirements. Abrasive water jet (AWJ) is a primary candidate for high speed machining of difficult-to-cut materials. The AWJ process performance is sensitive to the online faults and non-optimal process parameters, necessitating efficient techniques for online process control. In this study, acoustic emission (AE) signals are used to monitor AWJ machining of stacked titanium-CFRP. Owing to the non-stationary nature of the AE signals, this work is focused on the precision-driven predictive approach in simultaneous time-frequency domain. The AE signals were analyzed using wavelet packet transform (WPT), and an algorithm was proposed to identify and characterize these signals. Thirty-five different mother wavelets and decomposition levels up to 10 were used. The wavelet parameters (mother wavelet and decomposition) were deemed optimal when the identified signal characteristics could strongly correlate with the process parameters and kerf wall quality (surface roughness). Coiflets and Symlets were identified as the optimal wavelets with energy-entropy coefficient as the qualifying characteristic of the wavelet packet resulting in $R^2 > 90\%$. A comparative study was conducted to qualify the proposed algorithm against standard time domain analysis measures. The maximum R^2 and CV (RMSD)—coefficient of variation of root mean square deviation for time domain was observed as 88.6% and 12.5% respectively as opposed to $R^2 = 97.12\%$ and CV (RMSD) = 6% for the proposed WPT algorithm. Overall, an efficient algorithm was proposed in monitoring the process quality and controlling the process parameters based on the identified signal signatures.

Keywords Abrasive water jet · Titanium · CFRP · Stacks · Wavelet analysis · Process monitoring

Nomenclature

P	Hydraulic pressure
u	Jet traverse speed
$f(t)$	AE signal
ψ	Wavelet function
a	Scaling factor
g	Translation factor
h	Low-pass filter
g	High-pass filter
F_s	Sampling frequency
j	Decomposition level
TC_m	Ti/CFRP configuration, mth AE channel
CT_m	CFRP/Ti configuration, mth AE channel (m = 1 or 2)

✉ M. Ramulu
ramulum@uw.edu

Rishi Pahuja
rpahuja@uw.edu

[1] Department of Mechanical Engineering, University of Washington, Seattle, WA, USA

1 Introduction

Hybrid metal-composite material systems and structures are making strides in aerospace and automotive industry. Titanium (Ti6Al4V) and CFRP are among the primary candidates due to high-specific strength, modulus and toughness; less mismatch in coefficient of thermal expansion (CTE); and low electric potential preventing galvanic corrosion [1, 2]. Often times, secondary machining of stacked Ti6Al4V and CFRP is required either for drilling assembly holes or achieving dimensional tolerances. Machining of stacked Ti6Al4V and CFRP is challenging as both the materials not

only possess high strength but also belong to an entirely different class of materials. Titanium is reactive at high temperature and readily forms brittle oxide. Conventional machining results in residual stresses and exit burr formation [3]. Conventional machining of composites is dependent on the fiber orientation and often result in fraying, delamination, fiber pullouts, uncut and rebound fibers, and carcinogenic dust formation [4]. These machining induced damages and defects affect the surface and structural integrity of the machined component. Besides, significant tool wear and elevated cutting temperature results in high production times with conventional machine tools. When Ti and CFRP are stacked together, the machining induced defects for both Ti and CFRP are compounded which limits the usage of higher machining speeds [5–8]. Among several other non-conventional machining methods, abrasive water jet (AWJ) is a high-speed alternative to conventional machining [9]. The process is environment friendly and devoid of thermal distortion. However, since the interacting tool is a slurry, its distortion and reduction in energy with the penetration depth is reflected on the kerf characteristics. The resulting kerf witnesses the variation in cross-sectional geometry and striations at high speeds [9, 10]. Besides, initial kerf curving due to abrasive frosting, embedment of abrasive particles [11], exit delamination in CFRP are resulted at non-optimal machining conditions [12–14]. The problem is challenging in stacked metal composite due to difference in material removal mechanisms and possible distortion in the jet structure at the interface [15–18]. Owing to the sensitive nature of this stacked Ti6Al4V-CFRP configuration, process monitoring seems to be a natural extrapolation to assist and enhance the machinability of such metal-composite hybrid structures.

Several authors have applied wavelet transform in signal classification and process control for non-stationary signals [19–22]. Efforts have been made in correlating processing conditions and resulting surface quality using signal signatures through wavelet analysis. Zahouani et. al [23] used 2D continuous wavelet transform to identify the manufacturing signature on the surfaces generated by different stages of finishing. Plaza et al. [24] studied the WPT analysis of force signals in CNC turning and identified WPT parameters for online control and real-time quality monitoring. Recently, Pahuja et al. [25] studied the force signals in conventional milling of unidirectional composites and correlated relative wavelet entropy with the surface quality and defects. In AWJ process monitoring, a few efforts have been made. Momber, Mohan, and Kovacevic [26, 27] and Hreha and Hloch et al. [28, 29] used FFT (fast fourier transform) and PSD (power spectral density) to determine the material removal behavior and surface quality. Lissek et al. [30] used burst analysis and a negative relationship between speed and burst count was observed. Sutowski et. [31] observed high PSD with low jet energy and low exposure conditions in machining Al 5051. Pahuja et al. [17] analyzed AE signals in time and frequency domain to characterize the process parameters and penetration depth of stacked Ti and CFRP. The time-domain analyses were limited by the location dependency of the sensors. Time-frequency spectrogram was used but was limited by the simultaneous resolution in time and frequency domain. Other challenges were high signal attenuation in CFRP and low signal to noise in the aggressive AWJ environment caused by the turbulent conditions at the metal-composite interface [18]. By the nature of the erosion mechanism, AWJ is a non-stationary process and to capture the dynamic behavior, better resolution in time and frequency domain is required [17, 26]. Wavelet transform provides evolving resolution in time and frequency with higher temporal resolution at high frequency. This enables capturing the transient behavior in any non-stationary process.

Owing to the difference in machining behavior of metal-composite stacks, the jet energy is reduced and jet coherency distorted when penetrating this stacked alliance. This results in the variation in kerf quality and necessitates an effective approach to monitor the surface roughness for both Ti and CFRP in the stacked configuration. To the best of authors' knowledge, no effort has been made in AE analysis using wavelet packet transform (WPT) in AWJ machining for multi-material configurations. In this study, an algorithm was proposed based on WPT to characterize the AE signals in Ti/CFRP and CFRP/Ti material configurations. Optimal wavelet parameters (decomposition level and mother wavelet) and signal features were identified based on their correlation with process parameters and surface quality. The outcome of this study would result in precise monitoring of surface quality and controlling of process parameters based on the AWJ process signature in AE signals, as identified by the proposed algorithm. The novelty and efficiency of the proposed approach was affirmed by the comparative assessment with the time domain analysis techniques.

2 Wavelet packet analysis

Wavelet transform is an efficient tool in signal processing to analyze signal content simultaneously in time and frequency domain. A wavelet $\psi_{a,b}(t)$ is a family of functions such that the starting function (mother wavelet) decomposes the signal resulting in downsampled coefficients. The successive decomposition generates time-frequency coefficient map. At each decomposition level, daughter wavelets are generated obtained through scaling and translation of the mother wavelet (as given by Eq. 1.) These wavelet functions

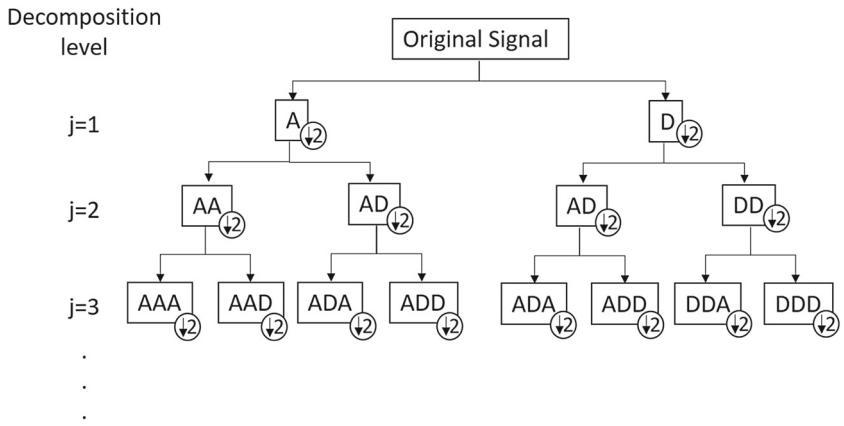

Fig. 1 Schematic illustration of wavelet packet decomposition

are analogous to the complex sinusoid in Fourier transform except that they exhibit some important properties, different from those complex sinusoidal functions. The wavelet functions oscillate about zero mean are not always smooth and can be asymmetric, while complex sinusoids are infinite in time, smooth, and predictable.

$$\psi_{a,b}(t) = \frac{1}{\sqrt{a}}\psi\left(\frac{t-b}{a}\right) \tag{1}$$

where b and a are translation and scale factors respectively such that $a \in \mathbb{R}^+$ where $\mathbb{R}$ is a real number. For continuous mathematically, continuous wavelet transform (CWT) is defined as the inner product of a given signal with the wavelet basis (as given by Eq. 2).

$$W_\psi f(a,b) = \langle f(t), \psi_{a,b}(t)\rangle$$
$$W_\psi f(a,b) = \frac{1}{\sqrt{a}}\int_{-\infty}^{\infty} f(t)\psi\left(\frac{t-b}{a}\right) \tag{2}$$

While CWT provides a fine and efficient time-frequency resolution, it carries redundant information in every step and is computationally intensive. To overcome the limitations of CWT, the discretized scales can be used. One form is dyadic discretization where the scales vary in the steps of $2^j (j = 1, 2, 3\cdots)$ Using the wavelets to allow multi-resolution analysis, two different tools have been developed—discrete

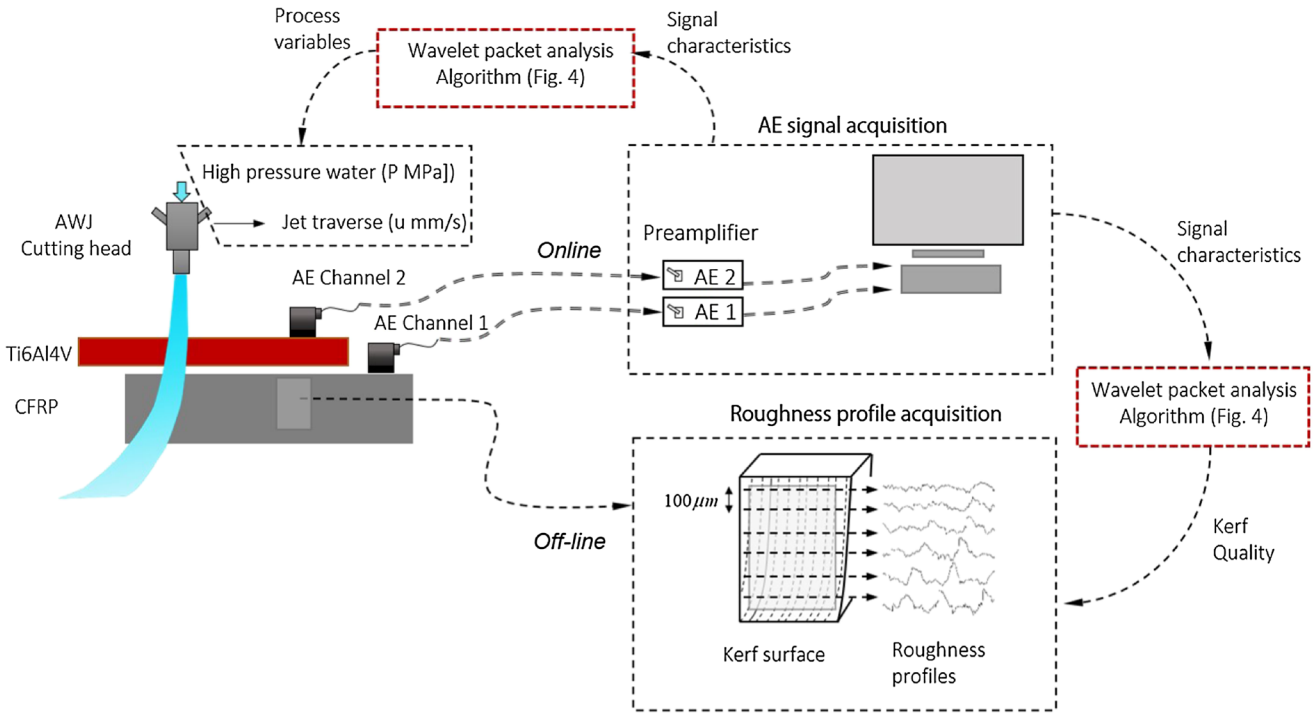

Fig. 2 Experimental set up and methodology

wavelet transform (DWT) and WPT. Each decomposition is carried out using the low- and high-pass functions, as described in Eqs. 3 and 4.

$$A_j(k) = \sum_n h(n-2k)c_{j-1} \tag{3}$$

$$D_j(k) = \sum_n g(n-2k)c_{j-1} \tag{4}$$

where A and B are approximation and detailed wavelet coefficients generated using low-pass (scaling) functions (h) and wavelet (high-pass) functions (g). j is the decomposition level ($j = 1, 2, 3\cdots$), $k = 1, 2, 3\cdots$ is the number of coefficients and is the total number of samples in original signal. Figure 1 schematically illustrates the decomposition procedure in WPT up to decomposition level 3. Starting with the original signal, the low-pass and high-pass filters decompose the signal into two sub-bands of approximation (scaling coefficients) and detailed coefficients (wavelet coefficients). The resulting approximation (A) sub-band has the low-frequency components and detailed (D) has high-frequency components. If the sampling frequency of the original signal is F_s, the frequency content of the two packets (sub-band) is [0, $F_s/4$) and ($F_s/4$, $F_s/2$]. Similarly for any jth decomposition level, 2^j wavelet packets (frequency sub-bands) are generated. These packets have the frequency range as follows:

$$\left[\frac{iF_s}{2^{j+1}}, \frac{(i+1)F_s}{2^{j+1}}\right)$$
$$i = 0, 1, 2\cdots 2^j - 1 \tag{5}$$

Therefore, after each decomposition, the signal is down sampled by two.

3 Methods and materials

In this study, stacked titanium-CFRP was machined in two configurations. Thickness of titanium (Ti6Al4V) and CFRP was 2.8 mm and 12.7 mm respectively. Flow International WJP 1313 AWJ system was used for the machining experiments. A ruby orifice and tungsten carbide nozzle was used with bore diameters of 0.33 mm and 0.9 mm respectively. Straight machining geometry was used and the experimental set up is shown in Fig. 2. The process variables were pressure (P) and traverse speed (u). Three pressure levels—200, 275, and 350 MPa and continuous traverse feed between 1 and 10 mm/s was used. The selection of parameters and their levels was based on the practical utility and the screening tests for partial depth penetration of the jet [18]. The design of experiments is given in and Table 1 respectively. Overall, 32 experimental conditions were used, 16 for each stacking configuration (Ti/CFRP and CFRP/Ti). As shown in Fig. 2, two wideband acoustic sensors (sampling frequency 1 MHz) were used with "AE-2"and "AE-1" channels at the top and bottom layer of the stack. The surface roughness of the machined kerf surface was recorded using Keyence VR3100 3D measurement system. 2D roughness profiles were further obtained from the 3D map using evaluation length, cutoff length (λ_c), and low-pass Gaussian filter (λ_s) 5.6 mm, 0.8 mm, and 25 μm respectively. The experimental methods and results are discussed in detail in the previous work [32].

Table 1 Experimental design in AWJ machining of Ti-CFRP and CFRP-Ti stacks [32]

Nomenclature	Pressure (MPa)	Speed (mm/s)	Stacking sequence
TC1	350	10	Ti/CFRP
TC2	350	7.5	Ti/CFRP
TC3	350	5	Ti/CFRP
TC4	350	4	Ti/CFRP
TC5	350	3	Ti/CFRP
TC6	350	2	Ti/CFRP
TC7	350	1	Ti/CFRP
TC8	275	10	Ti/CFRP
TC9	275	7.5	Ti/CFRP
TC10	275	5	Ti/CFRP
TC11	275	2	Ti/CFRP
TC12	275	1	Ti/CFRP
TC13	200	1	Ti/CFRP
TC14	200	5	Ti/CFRP
TC15	200	2	Ti/CFRP
TC16	200	7.5	Ti/CFRP
CT1	350	10	CFRP/Ti
CT2	350	7.5	CFRP/Ti
CT3	350	5	CFRP/Ti
CT4	350	4	CFRP/Ti
CT5	350	3	CFRP/Ti
CT6	350	2	CFRP/Ti
CT7	350	1	CFRP/Ti
CT8	275	10	CFRP/Ti
CT9	275	7.5	CFRP/Ti
CT10	275	5	CFRP/Ti
CT11	275	2	CFRP/Ti
CT12	275	1	CFRP/Ti
CT13	200	1	CFRP/Ti
CT14	200	5	CFRP/Ti
CT15	200	2	CFRP/Ti
CT16	200	7.5	CFRP/Ti

Table 2 Mother wavelets used in this study

Wavelet family	Order
Orthogonal	
Daubechies	db2, db3, db4, db5, db6, db7, db8, db9, db10
Coiflet	coif1, coif2, coif3, coif4, coif5
Symlet	sym2, sym3, sym4, sym5, sym6, sym7, sym8
Biorthogonal	bior1.3, bior1.5, bior2.2, bior2.4, bior2.6, bior2.8, bior3.1, bior3.3, bior3.5, bior3.7, bior3.9, bior4.4, bior5.5, bior6.8

3.1 Analysis methodology

The AE signals were analyzed using WPT. In order to extract any meaningful features from the signals, the selection of mother wavelet plays a critical role. The similarity in the profile anatomy with the mother wavelet can filter the *best* distinguishable feature(s). About 35 mother wavelets have been selected to analyze (as shown in Table 2). Figure 3 shows the physical shape of the mother wavelets of different orders and class used in this study. The first step in the analysis is the WPT of the given signal. For a given level of decomposition, the wavelet packets were calculated and arranged in increasing frequency order. Energy of each wavelet packet at that decomposition level is given by $f6$ in Table 3 where y_k is the k^{th} coefficient.

The total duration of the acquired signal was 30 s which has two zones: zone–a is when only top layer is machined and zone-b is when the stacked combination is machined. For WPT, a signal of 1.0-s duration was sampled from zone (b) due to overabundance in data. WPT was then applied to the sampled signals using 35 different mother wavelets and up to 10 decomposition levels. At the jth decomposition level, 2^j wavelet packets were generated and sorted in an increasing order of frequency range. Each wavelet packet was reconstructed and characterized with eight features, as described in Table 3. A total of 2^j packets were analyzed at the jth decomposition level. The calculated feature was plotted against a frequency-ordered wavelet packet number, and the peaks were detected which indicated dominant wavelet packets (frequency bands) for a given feature. The cumulative sum of the peak values at a jth decomposition level was used as an indicator to characterize the signal. Next, the step was repeated for 32 experimental conditions (16 conditions for each of the two staking configuration). The regression models were developed to relate the experimental conditions (pressure and traverse speed) with the calculated signal feature(s)/indicator. The multivariate regression involved a cubic model alongwith stepwise (forward and backward) selection method to eliminate the non contributing terms in the model. This step was repeated for 35 mother wavelets, 10 decomposition levels, and for eight different features. A total of 32 conditions resulted in 64 samples (one from each sensor). A total of $35 \times 10 \times 8 = 2800$ models were created for each stack configuration and each sensor which adds up to 11,200 models. The coefficient of determination (R^2), adjusted R^2, and RMSE (or CV(RMSD)) was calculated for each model. RMSE or RMSD is the root mean square error or root mean standard deviation and CV (RMSD) is the coefficient of variation of RMSE which is the ratio of RMSE and sample mean. The optimal wavelet conditions (mother wavelet, decomposition level, and feature) was selected based on certain criteria—maximum R^2, adjusted R^2, and minimum RMSE or CV(RMSD). Based on the selected wavelet conditions and features, the correlation between the process parameters and determined signal feature was established. Further to enable prediction and control of kerf wall surface quality, similar methodology was adopted except that the generated model utilized AE

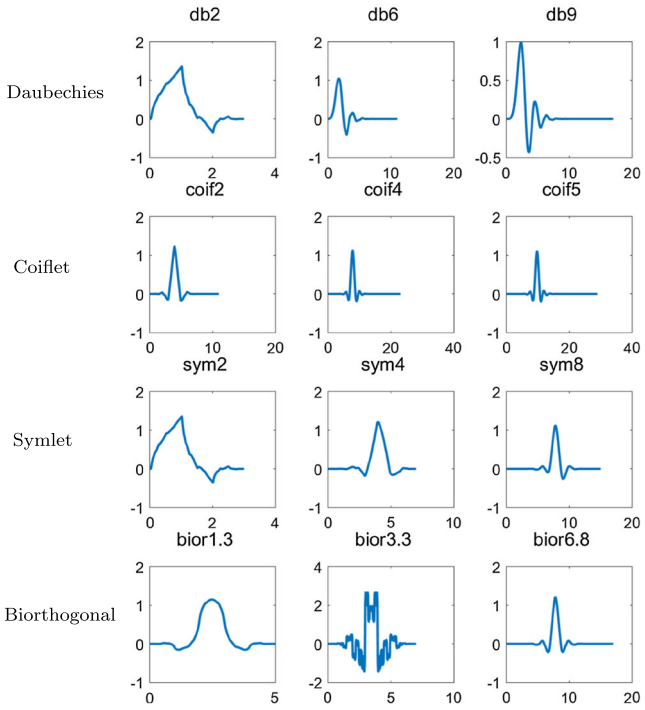

Fig. 3 Shape of mother wavelet **a** Daubechies, **b** Coiflet, **c** Symlet, and **d** Biorthogonal

Table 3 Features of wavelet packets

Feature	Nomenclature	Relation
Absolute mean	$f1$	$\bar{C}_i = \sum_{k=1}^{K} \lvert y_k \rvert$
Maximum peak-to-valley	$f2$	$\max(y_k) - \min(y_k)$
Root mean square	$f3$	$\sqrt{\frac{\sum_{k=1}^{K} y_k^2}{K}}$
Skewness	$f4$	$RSk_i = \frac{1}{\sigma_i^3 K} \sum_{k=1}^{K} (y_k - \bar{y}_i)^3$
Kurtosis	$f5$	$RKu_i = \frac{1}{\sigma_i^4 K} \sum_{k=1}^{K} (y_k - \bar{y}_i)^4$
Packet energy	$f6$	$E_i = \sum_{k=1}^{K} y_k^2$
Entropy	$f7$	$En_i = -\sum_{k=1}^{K} \frac{y_k^2}{E_i} log(\frac{y_k^2}{E_i})$
Energy-entropy coefficient	$f8$	$\eta_i = \frac{E_i}{En_i}$

signal from both sensors to predict the maximum surface roughness (R_z) in a given workpiece. The correlation between signal features extracted using optimal wavelet con dition and maximum R_z is auxiliary to the quality control. The process algorithm is summarized as the flowchart in Fig. 4.

4 Results and discussion

4.1 Kerf surface

Figure 5 shows the optical micrographs of kerf surfaces generated for TC8–TC12 and CT8–CT-12 experimental

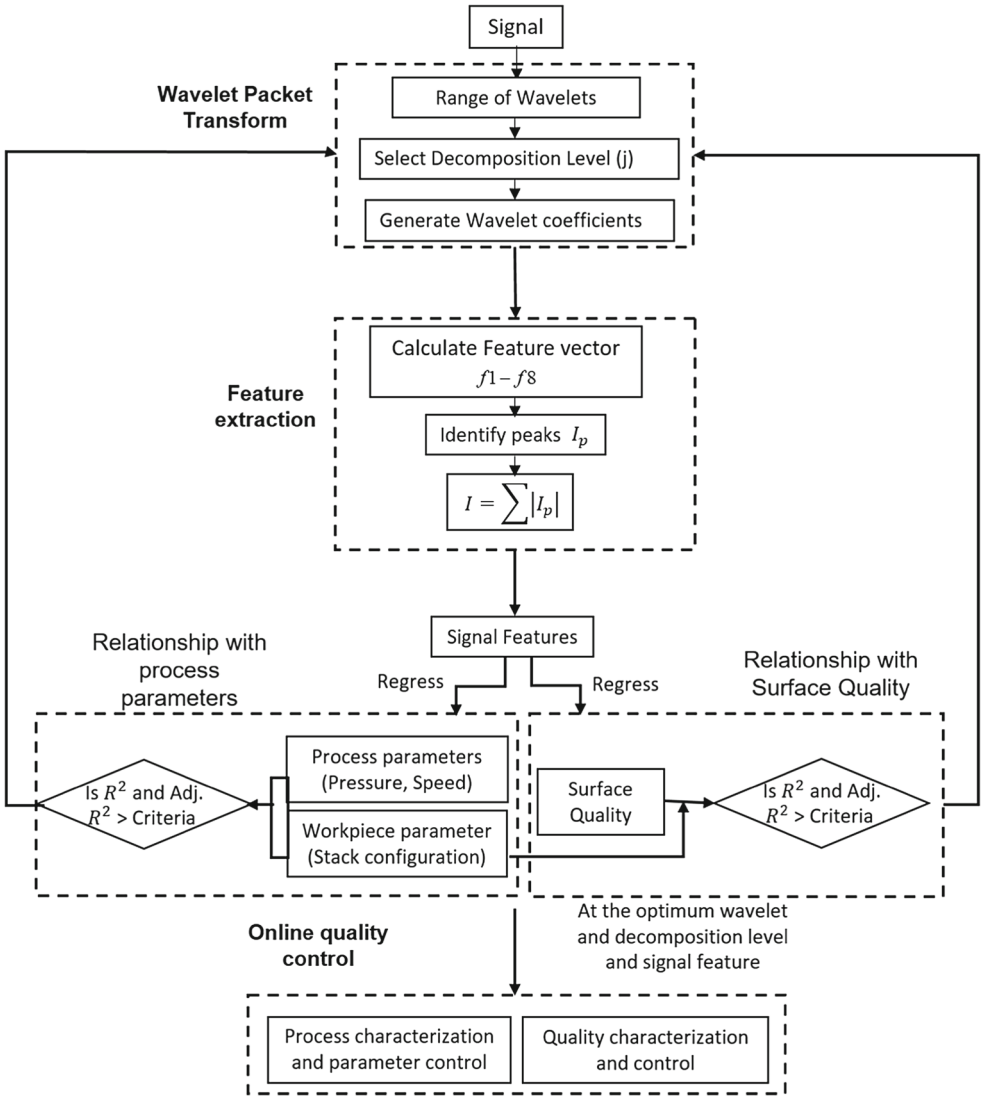

Fig. 4 Flowchart for the proposed WPT analysis algorithm

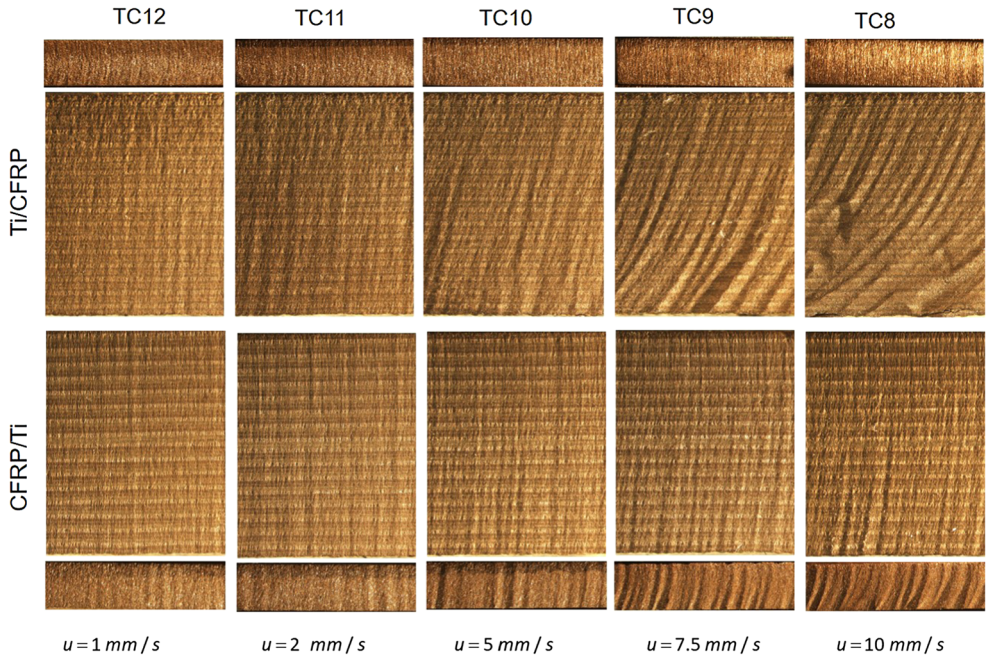

Fig. 5 Optical micrographs of surfaces generated in a AWJ-machined Ti/CFRP and CFRP/Ti stack at P = 275 MPa

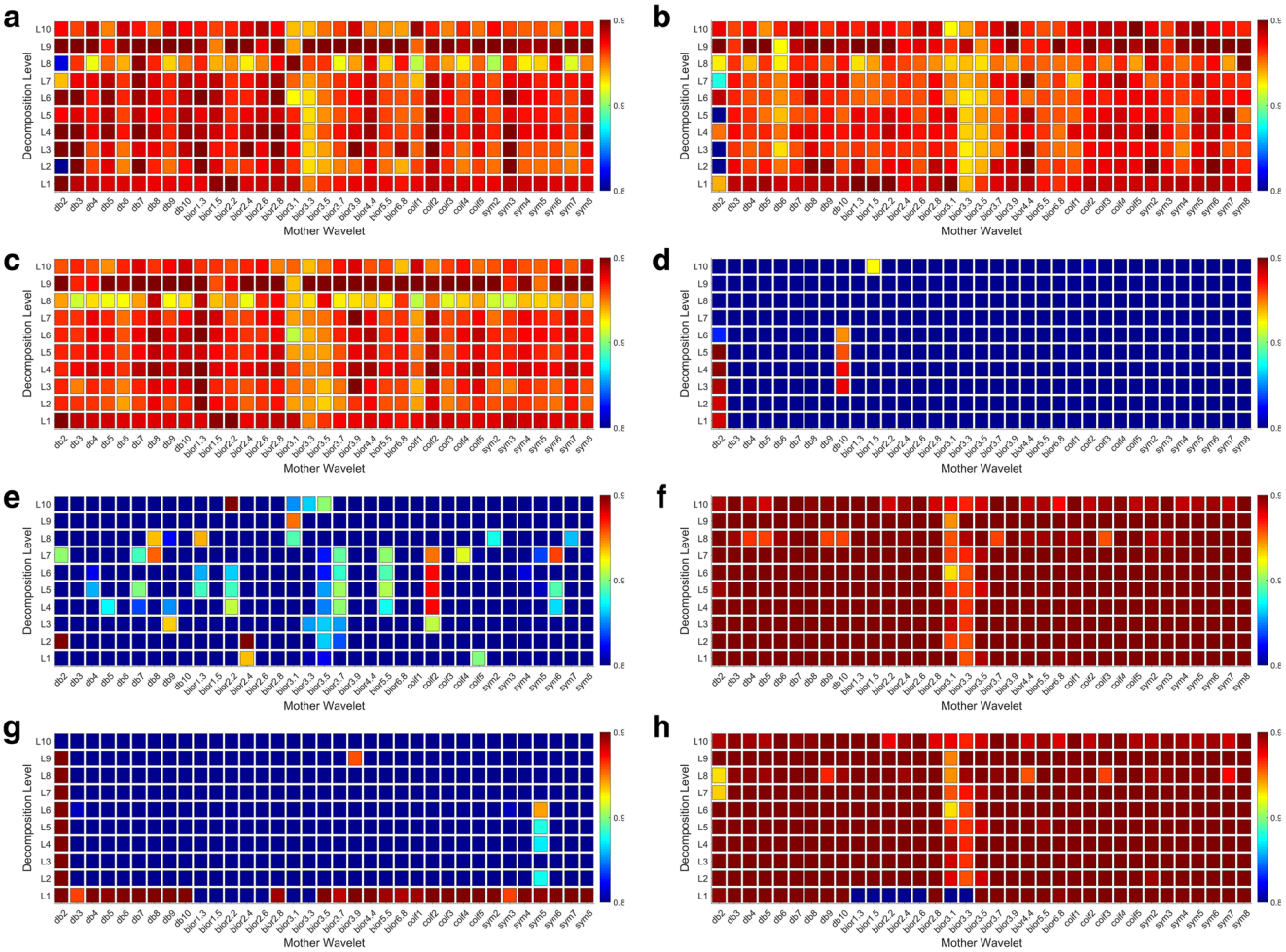

Fig. 6 R^2 for regression models developed using wavelet packets from decomposition level 2 to 10 for AE_1, TC condition determined using feature **a** f1, **b** f2, **c** f3, **d** f4, **e** f5, **f** f6, **g** f7, and **h** f8

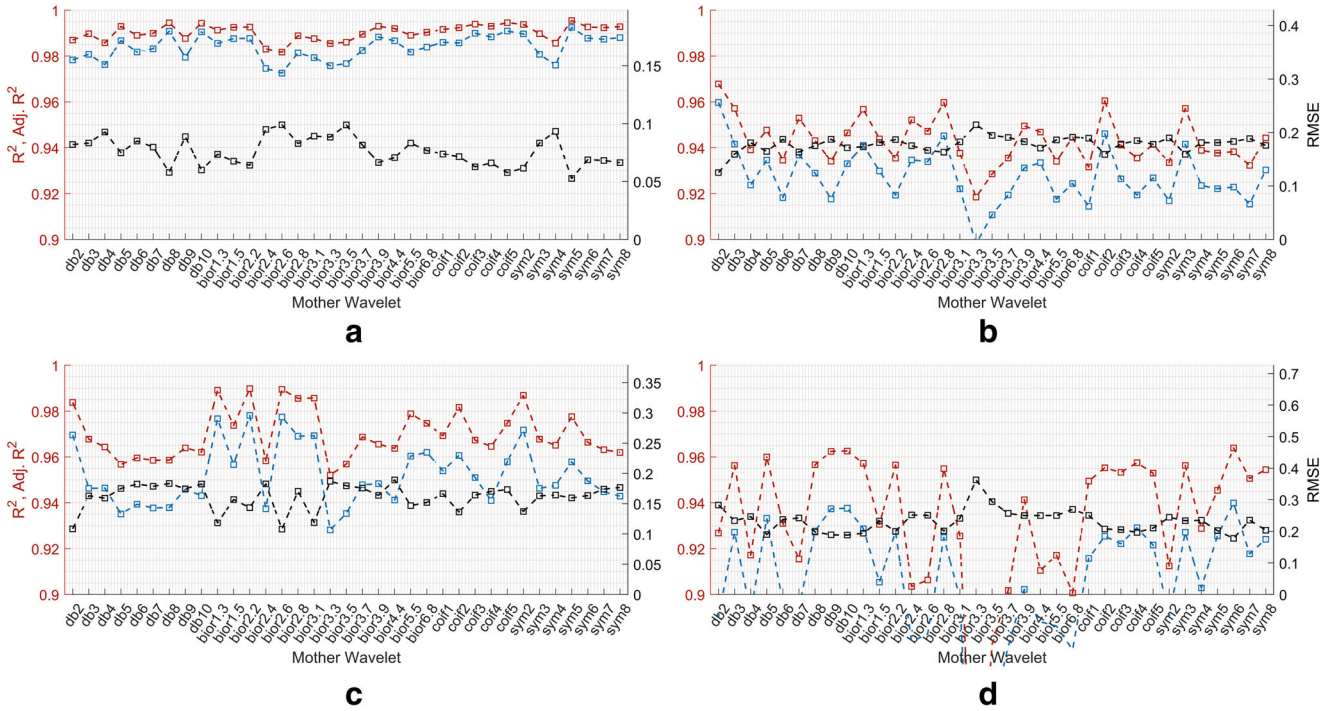

Fig. 7 Maximum R^2, adjusted R^2, and RMSE for regression models developed using feature—f1 (absolute mean) with wavelet packets from decomposition level 2 to 6 for **a** TC_2, **b** TC_1, **c** CT_2, and **d** CT_1 AE sensors

conditions mentioned in Table 1. At a given pressure, as the jet traverse speed increased, the backward bending of cutting front resulted in high striations on the kerf surface. This observation was consistent regardless of the stacking sequence of Ti and CFRP. The maximum 2D surface roughness was observed towards the jet exit side (bottom edge of the kerf) where jet curving and resulting loss in cutting energy is maximum. Within the given experimental conditions, the range of average roughness R_a was 1.8–17 μm and 1.89–11.6 μm for Ti and CFRP respectively.The maximum R_a observed for Ti/CFRP in Ti was 4.56 μm with a corresponding R_a of 6.67 μm in CFRP at TC2 condition (P = 350 MPa, u = 7.5 mm/s). The maximum R_a observed for Ti/CFRP in CFRP was 11.6 μm with a corresponding R_a of 4.05 μm in Ti at TC9 condition (P = 275 MPa, u = 7.5 mm/s). The maximum R_a in CFRP-Ti configuration was at TC1 condition (P = 350 MPa, u = 10 mm/s) with R_a = 7.33 μm–10.1 μm (CFRP–Ti) and also at TC8 condition (P = 275 MPa, u = 10 mm/s) with R_a = 6.24 μm–17 μm (CFRP–Ti). The kerf wall roughness and taper results are discussed in detail in the previous work [32].

4.2 Relationship with process parameters

Upon WPT of signals, the features mentioned in Table 3 were calculated and regressed with the process conditions—pressure and speed. A stepwise linear regression model was used with maximum degree of 3 for each predictor (P and u) in the initial model. An F-statistic was used to add or reject the potential predictor terms in the model according to SSE (sum of squares) criterion. This means that if a term

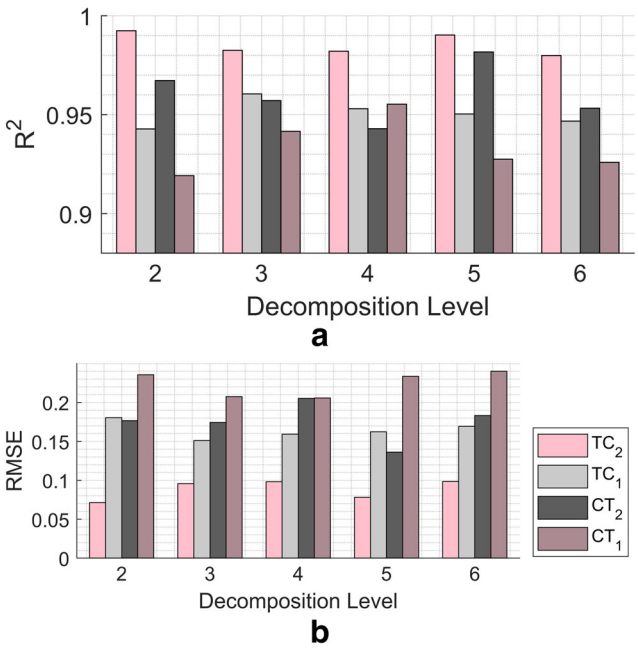

Fig. 8 R^2 decomposition level 2 to 6 for regression models calculated with selected feature (f1) and wavelet (coif2) for sensor **a** TC_2, **b** TC_1, **c** CT_2, and **d** CT_1 AE sensors

is not currently in the model, the null hypothesis is that the term would amount to zero coefficient if added to the model. However, a p value for those terms is calculated, and if qualifies (entry p value < 0.05), the null hypothesis is rejected and the term is added to the model. Similarly, if model currently has a term, the null hypothesis is that the term has zero coefficient. If qualifies (i.e., exit p value > 0.1), there is insufficient evidence to reject the null hypothesis and the term is removed from the model. A logarithmic transformation of the response variable was used to improve on the model statistics. Figure 6 shows the heat map for coefficient of determination when regressed with the AWJ process variable—pressure (P) and speed (u) for Ti/CFRP configuration for AE_1 signal. The abscissa of the map is the mother wavelet used to calculate WPT of the signal and ordinate is the decomposition level.

It was found that among all the features, absolute mean (f1), maximum peak-to-valley (f2), root mean square (f3), packet energy (f6), and energy-entropy coefficient (f8) were the competent candidates that could reasonably ($R^2 > 90\%$) correlate with the process parameters for all the sensor locations. The heat maps for other sensor location(s) and stacking configuration are not shown for the sake of brevity. Further, it was realized that satisfactory results could be obtained within decomposition level 6. Figure 7 shows the maximum R^2, adjusted R^2, and RMSE (root mean square error) regression models developed using wavelet packets with feature—f1 (absolute mean) from decomposition level 2 to 6 for (a) TC_2, (b) TC_1, (c) CT_2, and (d) CT_1 AE sensors respectively. As apparent, in Ti/CFRP configuration, the AE signal from top layer sensor correlated well with the process parameters for almost all mother wavelets with $R^2 > 0.97$ for most of the cases. However, only a few wavelets could effectively $R^2 > 94\%$ extract the features at the second layer (CFRP) in Ti/CFRP. On average, RMSE was less than 0.1 for top Ti layer while it was between 0.1 and 0.2 for the bottom CFRP layer. When the stacking sequence was reversed to CFRP/Ti, RMSE was between 0.1 and 0.2 from the top CFRP layer and between 0.15 and 0.4 for the bottom Ti layer. This confirms the response from the high-speed particle interaction with metal is more distinguishable than interaction with CFRP when at the top in stacking sequence. High R^2 could be obtained in CFRP but for selective wavelet parameters. As the jet cutting ability degrades with penetration depth, the correlation is more contingent upon the wavelet parameter selection, more so when titanium is at the bottom. The poor relation between signal features and process parameters at bottom titanium is a possible effect of (1) reduction in jet density and (b) reverse flow

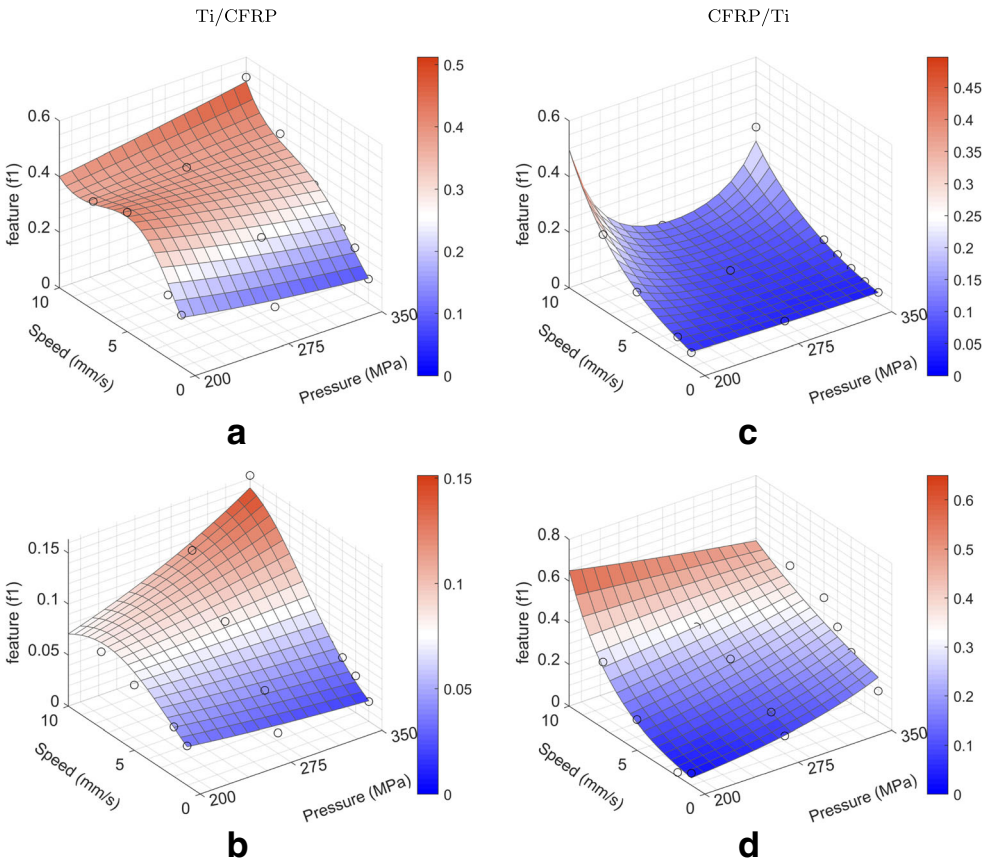

Fig. 9 R^2 Relationship between process variables and signal feature f1 determined with optimal wavelet conditions for sensor **a** TC_2, **b** TC_1, **c** CT_2, and **d** CT_1 AE sensors

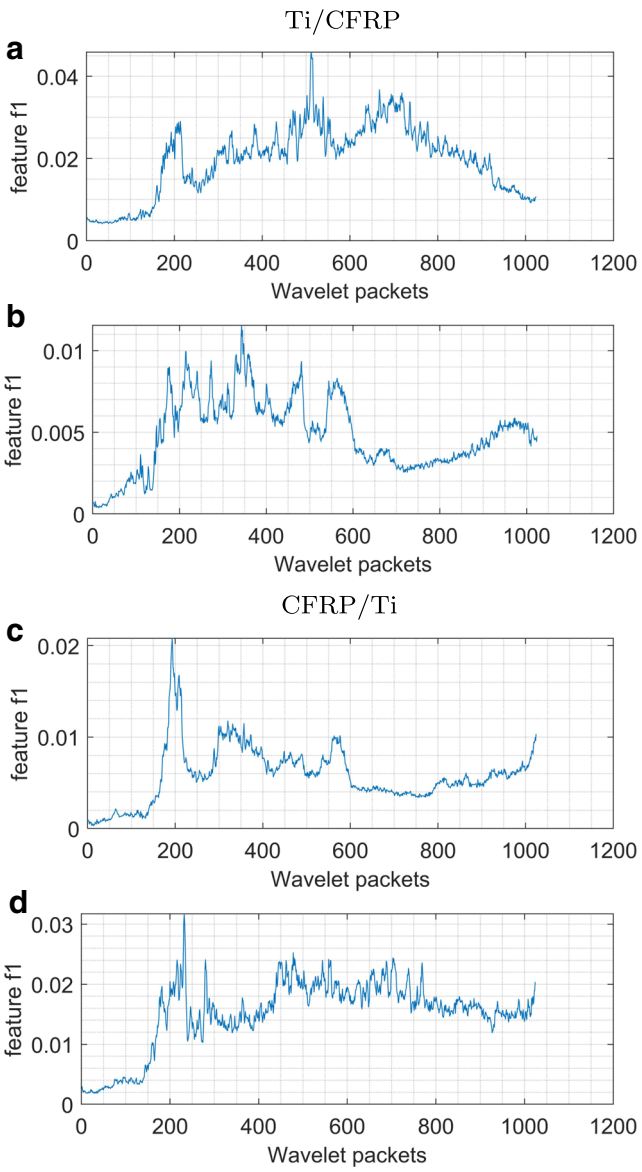

Fig. 10 Feature $f1$ versus wavelet packets determined at decomposition level 10 with coiflet-2 wavelet for experimental conditions TC2 and CT2: **a** TC_2, **b** TC_1, **c** CT_2, and **d** CT_1 AE signals

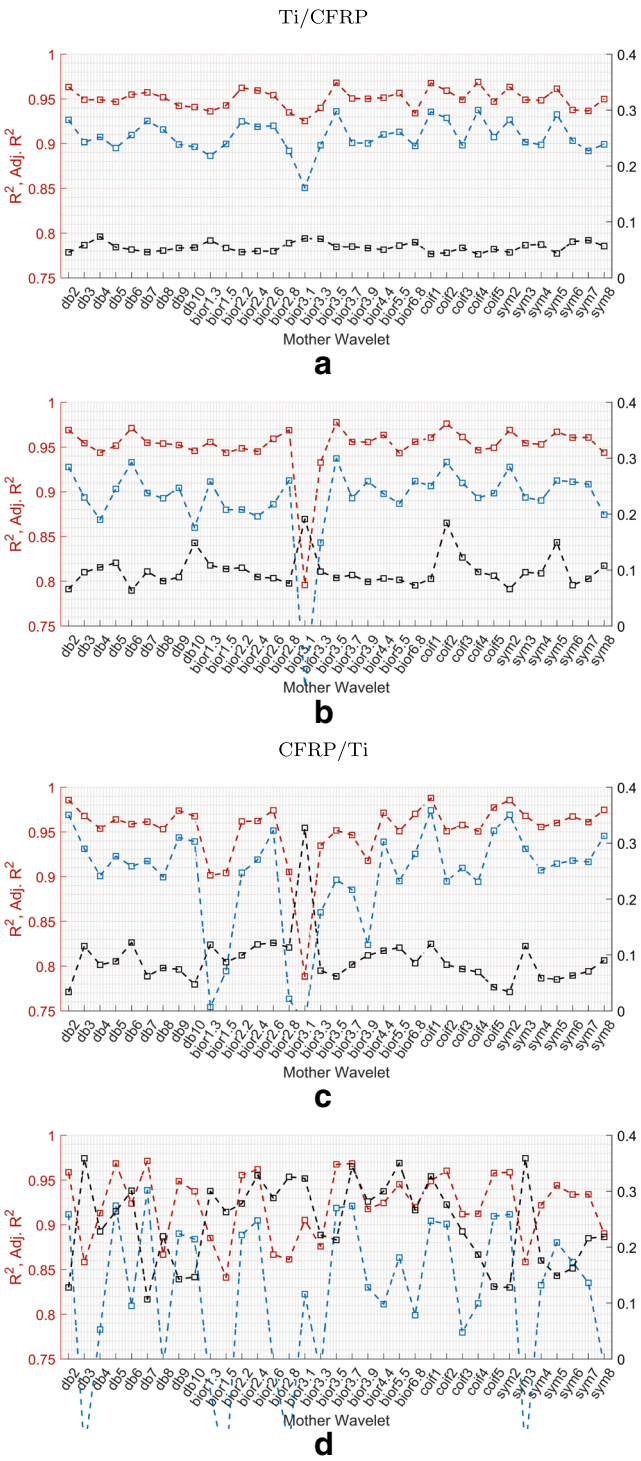

Fig. 11 Maximum R^2, adjusted R^2, and CV(RMSD) for regression models developed using wavelet packets from decomposition level 2 to 10 for **a** Ti in TC, **b** CFRP in TC, **c** CFRP in CT, and **d** Ti in CT

(and resulting high turbulence) due to sudden interaction from a material of low resistance to high resistance. For Ti/CFRP configuration, wavelets that resulted in a reasonable correlation were Bior1.3, 2.2, 3.1, Sym2, and Coif2. In CFRP/Ti configuration, db2, db5, db7, bior1.3, bior2.8, Coif2, and Sym3 were significant for top CFRP. For bottom, Ti, db3, db5, db9, db10, bior2.8, boif2-5, Sym3, and Sym8 were statistically significant. Among all, coiflet-2 was selected as the mother wavelet. Next, the decomposition level was selected based on maximum R^2 and minimum RMSE. Figure 8 a and b shows the R^2 and RMSE for decomposition levels 2 to 6 for the selected wavelet and feature $f1$. It was again observed that the performance of CT_1 signal was poor at levels where other signals perform adequately. At this point, different decomposition levels may be chosen for higher accuracy; however, for the sake of simplicity and comprehensibility, one level is selected.

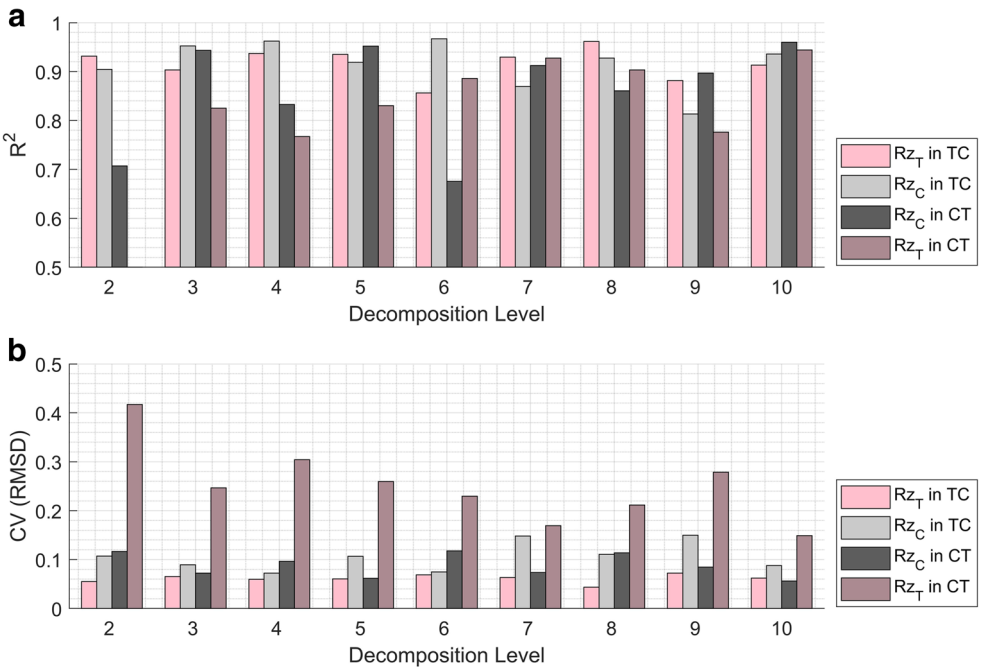

Fig. 12 R_z—signal feature (f8) model statistics **a** R^2 and **b** CV (RMSD) for decomposition level 2–10 with features calculated using Sym5 mother wavelet

Going forward, level 3 was selected for the analysis since lower decomposition level is computationally inexpensive. Figure 9 shows the relationship between process variables (pressure and speed) and selected signal feature ($f1$) determined using optimal wavelet conditions (Coiflet-2, level-3). In general, the most contributive factor was traverse speed followed by hydraulic pressure. For Ti/CFRP configuration, increment in traverse speed resulted in high $f1$ value. The effect of pressure was negligible at low speed, but at high speed, a positive trend was observed with $f1$. In CFRP/Ti configuration, a positive trend was observed with speed while the effect of pressure is not well captured.

To further investigate the physical significance of the signal signature, feature $f1$ was plotted against the wavelet packet number for decomposition level 10 and coiflet 2. Figure 10 shows the $f1$ as a function of frequency-ordered wavelet packets. At decomposition level 10 , $2^{10} = 1024$ wavelet packets were generated. As evident, the absolute mean feature has several dominant peaks while CFRP response is more compacted.

4.3 Correlation with surface roughness

Once the correlation between signal features and control variables have been identified and established, it is also important to identify signal features that affect the surface quality of the machined kerf wall. In contrast to the previous section where correlation between process parameters and signal features was independently for each sensor signal, the roughness correlation a multi-sensor approach for a given staking configuration. The maximum 2D roughness R_z parameters in each member of a given stack configuration was considered. Signal features from both the sensors were used as the predictors and maximum R_z as the response variable. Stepwise selection and removal of model terms were according to F-statistics, and a p value was 0.05 and 0.1 for entry and exit statistics. Quadratic mathematical models were developed and the heat maps were generated which are not included for the sake of brevity. This time, absolute mean (f1) and energy-entropy coefficient was successful in predicting the roughness behavior with $R^2 >$ 95%. Figure 11 shows the maximum R^2, adjusted R^2, and coefficient of variation of RMSD for decomposition levels 1–10 calculated with feature f1. As can be observed, CV (RMSD) was minimum (< 0.8) for Ti6Al4V in Ti/CFRP followed by CFRP in Ti/CFRP. Next, CFRP in CFRP/Ti resulted in CV(RMSD) < 0.85 which was mostly greater than 0.85 for Ti6Al4V in Ti/CFRP configuration.

Moving forward, Symlet–5 and feature f8 was selected as the optimum mother wavelet based on its high R^2 and low CV (RMSD). Figure 12 shows (a) R^2 and (b) CV (RMSD) for optimal wavelet parameters at decomposition levels 2–10. As evident, level 10 resulted in high R^2 and reasonably low CV (RMSD) for roughness prediction in both layers in both stacking configuration. Feature f1 also provided reasonable correlation but resulted in different optimal wavelet parameters for different stacking configuration. For Ti/CFRP configuration, it was Sym2 wavelet and level-5 decomposition while it was Sym5 and level 4 decomposition for CFRP/Ti configuration.

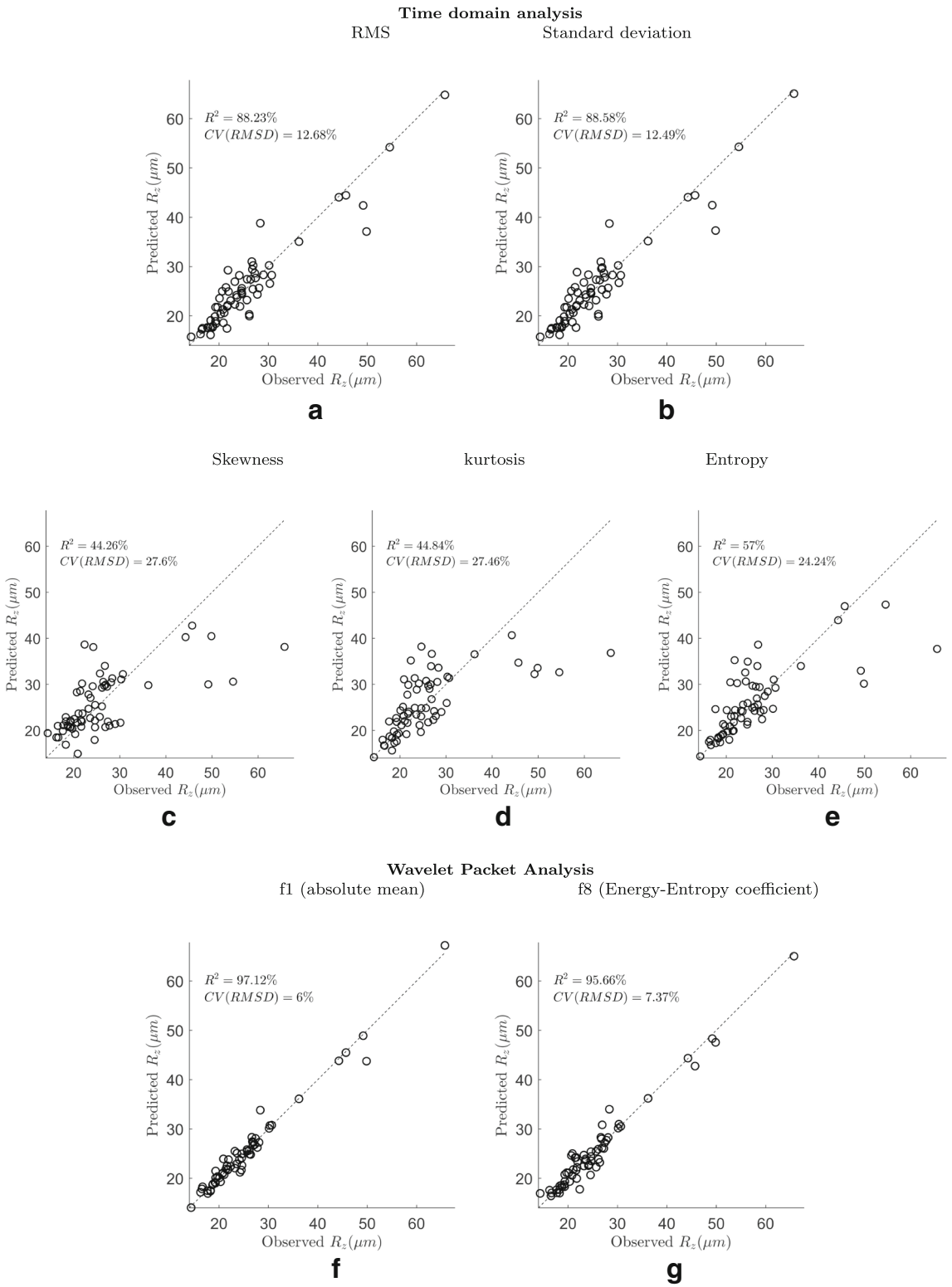

Fig. 13 Predicted vs. observed R_z with prediction calculated using averaged time domain **a** RMS, **b** standard deviation, **c** skewness, **d** kurtosis, **e** entropy, and wavelet packet using optimal wavelet conditions for feature **f** f1 (absolute mean) and **g** f8 (energy-entropy coefficient)

4.3.1 Comparison of models

Previous work [17] has demonstrated the techniques in time and frequency domain to correlate AE signal characteristics better with the process conditions. To determine and compare the features and methods that helps in better prediction of surface roughness parameter (R_z), the signal was windowed with a duration of 0.01 s each and a few features were determined. These time varying features were average RMS, standard deviation, skewness, kurtosis and entropy. From wavelet packet analysis, f1 (absolute mean) and f8 (energy-entropy coefficient) were selected. A quadratic, stepwise linear regression model was developed for each stacking sequence. Similar to the ANOVA in WPT, features of signals acquired from both top and bottom layers of the stack were used as predictors for maximum R_z in both layers. The p entry value was 0.05 and p exit was 0.1.

The combined results for observed vs. predicted roughness is plotted in Fig. 13. Among time-domain analysis, RMS, and standard deviation were the best estimators with $R^2 = 88.23\%$ and 88.58% respectively, and CV (RMSD) = 12.68% and 12.25% respectively. The features skewness and kurtosis resulted in $R^2 < 44.84\%$ with CV (RMSD) > 27.46%. Also, entropy was slightly better with $R^2 = 57\%$ and CV (RMSD) = 24.24%. Figure 13 a–e shows the predicted vs. observed R_z in time-domain analysis. This means RMS and standard deviation can be employed in roughness prediction. However, skewness vs. kurtosis, entropy, and cloud characteristics were effectively used in characterizing and clustering the signals. Figure 13 shows the prediction against the observed surface roughness in both experimental configurations. The prediction using feature f1 showed R^2 and CV(RMSD) of 97.12% and 6% respectively while it was $R^2 = 95.66\%$ and CV (RMSD) = 7.37% for feature f8. Clearly, WPT was superior over other methods.

5 Summary and conclusion

In this study, acoustic emission signals were analyzed to predict the surface quality in abrasive water jet machining of a stacked titanium-CFRP hybrid structure. A novel approach was proposed to decompose the signals using wavelet packet transform and extract characteristic features that can optimally describe the relationship between process parameters and kerf quality of the machined workpiece. A compendium of 35 mother wavelets and decomposition levels up to 10 were used to identify the wavelet decomposition parameters based on high R^2, low RMSE, and less computation power requirement (low decomposition level). Besides, several statistical features were extracted such as absolute mean, maximum peak-to-valley height, skewness, kurtosis, entropy, and energy-entropy coefficient. These features were used to determine relationship with process parameters and resulting surface quality. Using this proposed multi-scaled wavelet packet decomposition technique, following conclusions were made:

1. The maximum roughness R_a and R_z was observed at high traverse speed ($u > 7.5$ mm/s) at each pressure level, regardless of the stacking configuration. The roughness R_z was as high as 11.6 μm in Ti/CFRP (at P = 275 MPa, u = 7.5 mm/s), while it was 17 μm in CFRP/Ti configuration (at P = 275 MPa, u = 10 mm/s). Regression models were developed to select the optimal features, wavelet decomposition level and mother wavelet that help establish correlation with process parameters and surface quality.
2. Among the statistical features, absolute mean ($f1$), packet energy ($f6$), and energy-entropy coefficient ($f8$) were determined as optimal features to describe the process performance with $R^2 > 90\%$.
3. In determining the signal signature in relation with process parameters, Coiflet-2 and level 3 was identified as optimal wavelet parameter. In general, R^2 was higher for AE signals acquired at the top layer, especially in Ti/CFRP configuration.
4. Prediction of surface quality required a dual sensor approach which means the signal signatures from both the sensors were used simultaneously to generate predictive models for surface roughness. Symlet-5 and energy-entropy coefficient ($f8$) resulted in roughness prediction with $R^2 > 95\%$. The optimal decomposition level was 5 and 4 for Ti/CFRP and CFRP/Ti configuration respectively.
5. Upon comparing with the time domain analysis, WPT was found to be superior in predicting maximum roughness (R_z) in the specimens with $R^2 = 97.12\%$ and CV (RMSD) = 6%.

Acknowledgments This research was supported by the Boeing-Pennell Professorship funds. Authors sincerely acknowledge the support and encouragement of Dr. M. Hashish, Senior Technical Fellow at Flow International during the investigation.

Funding information This research was supported by the Boeing-Pennell Professorship funds.

References

1. Peng Z, Nie X (2013) Galvanic corrosion property of contacts between carbon fiber cloth materials and typical metal alloys in an aggressive environment. Surf Coat Technol 215:85–89
2. Fink A, Kolesnikov B (2005) Hybrid titanium composite material improving composite structure coupling. In: Spacecraft structures, materials and mechanical testing 2005, vol 581

3. Rahman M, Wang ZG, Wong YS (2006) A review on high-speed machining of titanium alloys. JSME Int J Ser C Mech Syst Mach Elem Manuf 49(1):11–20
4. Ramulu M (1997) Machining and surface integrity of fibre-reinforced plastic composites. Sadhana 22(3):449–472
5. Kim D, Ramulu M (2007) Study on the drilling of titanium/graphite hybrid composites. J Eng Mat Tech 129(3):390–396
6. Fernández-Pérez J, Cantero J, Díaz-Álvarez J, Miguélez M (2019) Hybrid composite-metal stack drilling with different minimum quantity lubrication levels. Materials 12(3):448
7. Ramulu M, Spaulding M (2016) Drilling of hybrid titanium composite laminate (HTCL) with electrical discharge machining. Materials 9(9):746
8. Pramanik A, Littlefair G (2014) Developments in machining of stacked materials made of CFRP and titanium/aluminum alloys. Mach Sci Tech 18(4):485–508
9. Hashish M (1989) A model for abrasive-waterjet AWJ machining. J Eng Mater Tech 111(2):154–162
10. Chen F, Siores E (2003) The effect of cutting jet variation on surface striation formation in abrasive water jet cutting. J Mater Process Tech 135(1):1–5
11. Fowler G, Pashby I, Shipway P (2009) The effect of particle hardness and shape when abrasive water jet milling titanium alloy Ti6Al4V. Wear 266(7-8):613–620
12. Ramulu M, Wern C, Garbini J (1993) Effect of fibre direction on surface roughness measurements of machined graphite/epoxy composite. Compos Manuf 4(1):39–51
13. Ramulu M, Arola D (1994) The influence of abrasive waterjet cutting conditions on the surface quality of graphite/epoxy laminates. Int J Mach Tool Manuf 34(3):295–313
14. Pahuja R, Ramulu M (2016) Machinability of randomly chopped discontinuous fiber composites: a comparative assessment of conventional and abrasive waterjet. In: The 23rd int conf on water jetting. Seattle, USA, pp 127–148
15. Pahuja R, Ramulu M, Hashish M (2014) Abrasive water jet machining (AWJ) of hybrid titanium/graphite composite laminate. In: 22nd Int Conf on Water Jetting 2014: advances in current and emerging markets, BHR Group Limited
16. Alberdi A, Artaza T, Suárez A, Rivero A, Girot F (2016) An experimental study on abrasive waterjet cutting of CFRP/Ti6Al4V stacks for drilling operations. Int J Adv Manuf Tech 86(1-4):691–704
17. Pahuja R, Ramulu M (75) Abrasive waterjet process monitoring through acoustic and vibration signals. In: 24th Int conference on water jetting 2014, BHR Group Limited
18. Pahuja R, Ramulu M (2019) Abrasive water jet machining of titanium (Ti6Al4V)–CFRP stacks–a semi-analytical modeling approach in the prediction of kerf geometry. J Manuf Process 39:327–337
19. Safara F, Doraisamy S, Azman A, Jantan A, Ramaiah ARA (2013) Multi-level basis selection of wavelet packet decomposition tree for heart sound classification. Comput Biol Med 43(10):1407–1414
20. Rosso OA, Blanco S, Yordanova J, Kolev V, Figliola A, Schürmann M, Başar E (2001) Wavelet entropy: a new tool for analysis of short duration brain electrical signals. J Neurosci Methods 105(1):65–75
21. Zhang Z, Li H, Meng G, Tu X, Cheng C (2016) Chatter detection in milling process based on the energy entropy of VMD and WPD. Int J Mach Tools Manuf 108:106–112
22. Patra K, Pal SK, Bhattacharyya K (2007) Application of wavelet packet analysis in drill wear monitoring. Mach Sci Technol 11(3):413–432
23. Zahouani H, Mezghani S, Vargiolu R, Dursapt M (2008) Identification of manufacturing signature by 2D wavelet decomposition. Wear 264(5-6):480–485
24. Plaza EG, López PN (2018) Analysis of cutting force signals by wavelet packet transform for surface roughness monitoring in CNC turning. Mech Syst Signal Process 98:634–651
25. Pahuja R, Mamidala R (2018) Process monitoring in milling unidirectional composite laminates through wavelet analysis of force signals. Procedia Manuf 26:645–655
26. Momber AW, Mohan RS, Kovacevic R (1995) Acoustic emission measurements on brittle materials during abrasive waterjet cutting. Tech papers - SME
27. Kovacevic R, Kwak H, Mohan R (1998) Acoustic emission sensing as a tool for understanding the mechanisms of abrasive water jet drilling of difficult-to-machine materials. Proc IMechE, Part B: J Eng Manuf 212(1):45–58
28. Hreha P, Hloch S, Perzel V (2012) Analysis of acoustic emission recorded during monitoring of abrasive waterjet cutting of stainless steel AISI 309. Tehnicki Vjesnik 19(2):355–359
29. Hreha P, Radvanská A, Hloch S, Peržel V, Królczyk G, Monková K (2015) Determination of vibration frequency depending on abrasive mass flow rate during abrasive water jet cutting. Int J Adv Manuf Tech 77(1-4):763–774
30. Lissek F, Kaufeld M, Tegas J, Hloch S (2016) Online-monitoring for abrasive waterjet cutting of CFRP via acoustic emission: Evaluation of machining parameters and work piece quality due to burst analysis. Procedia Eng 149:67–76
31. Sutowski P, Sutowska M, Kapłonek W (2018) The use of high-frequency acoustic emission analysis for in-process assessment of the surface quality of aluminium alloy 5251 in abrasive waterjet machining. Proc IMechE, Part B: J Eng Manuf 232(14):2547–2565
32. Pahuja R, Ramulu M, Hashish M (2019) Surface quality and kerf width prediction in abrasive water jet machining of metal-composite stacks. Composites Part B: Eng: 107–134 https://doi.org/10.1016/j.compositesb.2019.107134